Materials Science & Engineering A 801 (2021) 140405

Contents lists available at ScienceDirect

Materials Science & Engineering A

journal homepage: http://www.elsevier.com/locate/msea

Twinning in rolled AZ31B magnesium alloy under free-end torsion

Luiz Carneiro, Duke Culbertson, Qin Yu [**,1], Yanyao Jiang [*]

University of Nevada, Reno, Department of Mechanical Engineering, NV 89557, USA

ARTICLE INFO

Keywords:
Magnesium alloy
Torsion
Swift effect
Strain hardening
Twinning

ABSTRACT

The mechanical response and microstructure evolution in a rolled AZ31B magnesium alloy were experimentally characterized using companion thin-walled tubular specimens under free-end monotonic torsion. The tubular specimens were made with their axes along the normal direction of the rolled magnesium plate. The shear stress-shear strain response shows a subtle sigmodal shape that is composed of four distinctive stages of strain hardening. Basal slips and tension twinning are operated throughout the shear deformation. Both tension twinning and compressing twinning are favored. Growth and interaction of tension twins with multiple variants lead to formation of twin-twin boundaries (TTBs). The collective hardening effects by twin boundary (TB) and TTB result in a unique rise of the strain hardening rate in Stage II and III. In addition to primary twins, tension-compression double twins and tension-compression-tension tertiary twins with detectable sizes are observed in the tension-twin favorable grains whereas compression-tension double twins are detected in the tension-twin unfavorable grains; all of which become more observable with the increasing shear strain. During Stage IV deformation where TTB formation exhausts, non-basal prismatic slips become more significant and are responsible for the progressive decrease in strain hardening rate in this stage. Swift effect, which is commonly observed in textured materials, is evidenced under free-end torsion. The origin of Swift effect is confirmed to be dislocation slips at a shear strain less than 5% but is predominantly due to tension twinning at a larger plastic strain.

1. Introduction

Magnesium (Mg) alloys are potential structural materials for lightweight mechanical components due to their low specific weight [1]. However, the limited number of independent slip systems inherently associated with the hexagonal close pack (*hcp*) structure of Mg alloys limits the formability and ductility at room temperature [1–3]. The asymmetric nature of the *hcp* structure combined with the strong initial texture leads to the anisotropic mechanical behavior of the wrought Mg alloys. For instance, hot rolling generates a strong basal texture where most of the grains have their *c*-axes oriented parallel to the normal direction (ND) of the rolled Mg alloy plate.

The plastic deformation in Mg alloys is accommodated by both twinning and dislocation slips. The slip systems available in Mg are <*a*> basal, <*a*> prismatic, <*a*> pyramidal, and <*c*+*a*> pyramidal slips. The only slip system that is capable of accommodating deformation along the *c*-axis is <*c*+*a*> pyramidal slip which requires a high critical resolved shear stress (CRSS) to operate at room temperature [3]. Twinning is often operated instead of <*c*+*a*> pyramidal slips to accommodate plastic deformation along the *c*-axis because a much lower activation CRSS is required at room temperature. The most common twinning modes in magnesium are $\{10\bar{1}2\}\langle 10\bar{1}1\rangle$ tension twinning and $\{10\bar{1}1\}\langle 10\bar{1}\rangle$ compression twinning, which can accommodate extension and contraction along the *c*-axis, respectively.

Although the role of twinning in the deformation of Mg alloys has been extensively studied, most of the work has been focused on the mechanical behavior under uniaxial tension or compression. As a comparison, simple shear or torsion is considered as a more appealing experiment to investigate the plastic deformation of ductile materials as necking is absent at high levels of plasticity. Experimental work has been performed for Mg alloys subjected to simple shear [4–6], monotonic torsion [7–20], and cyclic torsion [10–12,21–26]. It has been shown that free-end torsion can induce an axial contraction of the extruded specimens [7–9,19], whereas an axial extension is resulted in the rolled specimen [14]. Such second order deformation along the axial direction during free-end torsion is termed as the Swift effect [27]. In Mg alloys,

* Corresponding author.
** Corresponding author.
E-mail addresses: qin.yu.unr@gmail.com (Q. Yu), yjiang@unr.edu (Y. Jiang).
[1] Current address: Materials Sciences Division, Lawrence Berkeley National Laboratory, Berkeley, CA, 94720, USA.

https://doi.org/10.1016/j.msea.2020.140405
Received 5 August 2020; Received in revised form 14 October 2020; Accepted 15 October 2020
Available online 17 October 2020

the Swift effect is mostly attributed to the operation of tension twins [14,28]. Regarding the dominant deformation mechanisms, numerical simulations indicate that basal slips, prismatic slips, and tension twinning play the major roles in torsion deformation of the extruded Mg alloy [8,14] whereas basal slips and tension twinning prevail in rolled Mg alloy subjected to torsion about the normal direction of the rolled plate [14]. Under cyclic torsion, symmetric stress-strain hysteresis loops are displayed [10–12,21,23–25,29] at high strain amplitudes, where twinning and detwinning occur simultaneously during both loading reversals [25,30]. Furthermore, it has been revealed that material processing through pre-torsion followed by annealing may improve the strength and ductility of Mg alloys under tension, compression, and cyclic tension/compression loading [9,16–18,31].

Limited experiments have been conducted involving free-end torsion of Mg alloys about the *c*-axis [14]. Most of the relevant studies used solid cylinder specimens, which is not ideal because the distribution of shear stress and strain along the radial direction on the cross-section is not uniform. In addition, a systematic investigation of the twinning evolution during free-end torsion is not currently available. To fill these gaps, the present study seeks to understand the role of twinning in the shear deformation in a wrought Mg alloy by carrying out free-end torsion of thin-walled tubular specimens machined from a rolled AZ31B Mg alloy plate with the tube axis aligning parallel to the plate normal. The torsional mechanical response and the associated microstructural evolution are characterized in detail to enlighten the dominant deformation mechanisms with an emphasis on the roles of deformation twins.

2. Material and method

The material used in this work is an AZ31B (Mg–3Al–1Zn) Mg alloy acquired in the form of a 76.2 mm thickness hot rolled plate. The initial microstructure was characterized on three orthotropic planes with their unit normal oriented in the rolled direction (RD), transverse direction (TD), and normal direction (ND) of the plate, respectively. Electron backscattered diffraction (EBSD) scans reveal that the rolled AZ31B is composed of mostly equiaxed grains with an average grain size of approximately 50 μm without showing apparent initial twins (Fig. 1). The material displays a strong texture, where most of the grains are oriented with their *c*-axes parallel to the ND of the rolled plate.

Thin-walled tubular specimens were machined from the rolled plate with their axial direction parallel to the ND of the plate (Fig. 1). The testing specimens have a 26 mm-long gage section with an outer diameter (d_o) of 24 mm and an inner diameter of 20 mm. The outer surface of the gage section was polished before testing using sandpapers with grit sizes ranging from P400 to P1000.

The free-end torsion experiment was performed using a servo-hydraulic axial-torsion fatigue testing system in ambient air. The machine has an axial load capacity of ±222 kN and a torsion load capacity of ±2800 Nm. The shear strain was measured by a modified biaxial MTS extensometer with a gage length of 25.4 mm and shear strain range of ±3%. Because of the limited range in the extensometer, the extensometer was removed after the shear strain reached ~4%. After the test was done, the residual plastic shear strain was measured based on the deformed angle between the axial and tangential lines engraved on the outer surface of the untested specimen. The shear strain after the extensometer removal was extrapolated assuming a linear relationship between the shear strain and the rotation angle measured by the rotary variable displacement transducer (RVDT) in the testing machine. All the experiments were conducted under rotation angle control at an angle rate of 0.7° s^{-1}, which was approximately equivalent to a shear strain rate of 0.005 s^{-1}. The shear stress and shear strain presented are values calculated at the mid-section of the tubular specimen assuming a linear distribution of the shear stress and the shear strain over the thickness of the specimen.

In order to characterize the microstructural evolution, companion specimens were unloaded at rotation angles of 5°, 10°, 20°, 30°, and 40°, corresponding to the mid-section plastic shear strains of 0.036, 0.069, 0.131, 0.191, and 0.254, respectively. The microstructure after deformation was analyzed employing electron-backscattered diffraction (EBSD). Cross-section samples were cut from the tested specimens with the scan plane perpendicular to the axial direction (Fig. 1). The sample surface was mechanically ground using SiC sandpapers down to P1200 grit size, followed by vibratory polishing using aluminum oxide with a particle size of 0.05 μm and etching with 3% Nital for 5 s. EBSD scans sized in 500×500 μm^2 were taken in a Joel 7100 F field emission scanning electron microscope (SEM) equipped with an Oxford HKL Channel 5 instrument at an acceleration voltage of 20 kV. The working distance and maximum step size were taken as 25 mm and 1.0 μm, respectively.

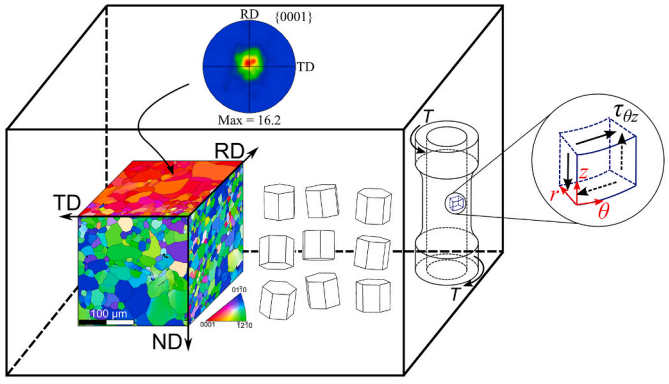

Fig. 1. Schematic illustration of the rolled AZ31B plate with an embedded thin-walled tubular specimen with the axis parallel to the ND of the plate. The three-dimensional EBSD stereograph reveals that the initial basal-textured microstructure is composed of equiaxed grains with an average grain size of ~50 μm.

3. Results and discussion

3.1. Mechanical response

The shear stress (τ), the axial strain(ε), and the plastic shear strain hardening rate ($d\tau/d\gamma_p$) as a function of plastic shear strain (γ_p) are presented in Fig. 2. Under free-end torsion, the shear modulus of the AZ31B alloy is measured to be 16.3 GPa, and the material yields at a shear stress of 34 MPa. The plastic shear strain at fracture attains as high as 26.6% corresponding to a shear stress of 111 MPa. In addition to the shear mechanical response, the torsion-induced Swift effect is clearly evidenced in Fig. 2, *i.e.,* an increasing axial strain is developed during free-end torsion, reaching a maximum value of 3.5% at fracture of the specimen. A subtle sigmodal shape can be observed when examining the shear stress-plastic strain curve carefully. This response can be visualized more clearly when the plastic shear strain hardening rate ($d\tau/d\gamma_p$) is plotted with respect to the shear strain, where four distinct stages are exhibited: Stage I—rapid decrease of $d\tau/d\gamma_p$ due to macroscopic yielding at $\gamma_p = \sim 0.2\%$; Stage II—fast resurgence of $d\tau/d\gamma_p$ from 250 MPa to 330 MPa ($3.2\% < \gamma_p < 5.3\%$); Stage III—slow increase of $d\tau/d\gamma_p$ from 330 MPa to 382 MPa ($5.3\% < \gamma_p < 12.0\%$); Stage IV—continuous decrease of $d\tau/d\gamma_p$ from 382 MPa to 147 MPa ($12.0\% < \gamma_p < 25.9\%$ at fracture). Deformation twins play an important role in the multi-stage strain hardening behavior, which will be discussed.

3.2. Microstructure evolution

Samples were cut from each companion specimen after being loaded to a designated strain level for characterizing the microstructure using EBSD. Unlike the uniaxial loading along the ND in a rolled plate, where tension twinning is favored under tension while compression twinning is

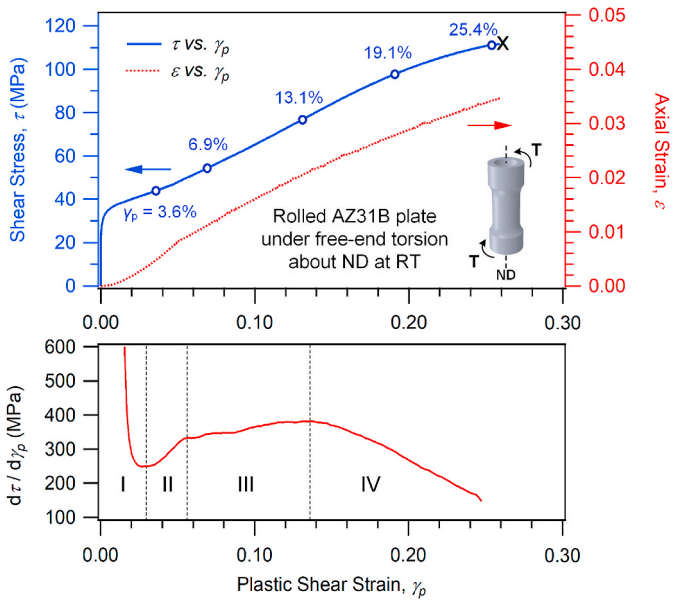

Fig. 2. Shear stress (τ), axial strain(ε), and plastic strain hardening ($d\tau/d\gamma_p$) as a function of plastic shear strain (γ_p) obtained from free-end torsion of rolled AZ31B about the ND. White circle marks indicate the companion specimen strain levels used for microstructural analysis. "X" denotes a final fracture.

promoted under compression, torsion about the ND leads to unique twinning behavior. To better understand the twinning favorability, the Schmid factors (SFs) of both tension twinning and compression twinning for all the possible grain orientations under pure shear stress state were calculated and these SF values were projected in the (0001) pole figures according to their crystal orientations, as shown in Fig. 3a. Note here that the shear stress,$\tau_{\theta z}$, is described in the local coordinates oriented in the radial (r), tangential (θ), and axial (z) axes, thereby the pole figures are presented on the θ-r plane. As shown in Fig. 3a, the SF pole figures under pure shear display the twinning SFs in opposite signs about the radial axis, *i.e.*, a misalignment of the c-axis about the r-axis by positive and negative rotations will lead to twinning SFs with opposite signs. To be specific (Fig. 3a), grain A with the c-axis slightly misaligned towards the negative θ–axis leads to a negative SF for $\{10\bar{1}2\}$ tension twinning (unfavorable for tension twinning), whereas grain B with the c-axis misaligned towards the positive θ–axis results in a positive SF for tension twinning (favorable for tension twinning); *vice versa* for the SF of compression twinning (Fig. 3a). The Schmid analysis was applied to the realistic grain orientations in the basal-textured AZ31B plate (Fig. 1) under pure shear about the ND. The results suggest that 70% of the grains have positive SFs and are favorable for $\{10\bar{1}2\}$ tension twinning. However, the remaining 30% grains that are not favorable for tension twinning actually enable the favorability for compression twinning. This indicates that tension and compression twins are both anticipated in the free-end torsion of the specimen under investigation.

The microstructural evolution is presented in Fig. 3b–e as a function of shear strains of 3.6%, 13.1%, 19.1%, and 25.4%, respectively. The EBSD results are presented in terms of the inverse pole figure (IPF) map, the pole figure, and the band contrast (BC) map with twin boundaries of different types highlighted in different colors. Symbol T_i (i=1–6) represents the individual $\{10\bar{1}2\}$ twin variant following the labeling convention in Ref. [32]. T_1 corresponds to the $(10\bar{1}2)$ $[\bar{1}011]$ variant, while increasing subscripts correspond to the other variants by counter-clockwise rotation about the c-axis. Symbol C_i denotes the $\{10\bar{1}1\}$ compression twin variants following the same labeling notation. Secondary and tertiary twins are represented by individual twin variants connected by dash line following the sequential order of activation. For example, T_i-C_j denotes a tension-compression double twin, where a secondary C_j compression twin formed in a primary T_i primary twin.

Also indicated in the IPF maps in Fig. 3b–e are the volume fractions for the tension twin (T-TVF) and the TVF for all the other twins. The TVF of a specific twin system was calculated as the ratio of the total twinned area of such a system to the total scanned area. For each twinned area, the specific twin system, whether a primary tension/compression twin or a secondary/tertiary twin (such as T-C, C-T, T-T, or T-C-T), was individually determined by examining the misorientation relationship between twin and parent as well as the variant analysis.

As shown in Fig. 3b, at a low shear strain level (γ_p=3.6%) which corresponds to the beginning of Stage-II strain hardening, $\{10\bar{1}2\}$ tension twins with only one variant that has the highest SF are developed in the grains oriented favorable for tension twinning, such as T_2 in grain G1. At γ_p=13.1% (Fig. 3c) near the end of the Stage-III strain hardening, tension twins with multiple variants are clearly visible in those favorable grains. Due to the growth of twins with different variants, twin-twin interaction is significantly promoted, forming a number of TTBs of both co-zone and non-co-zone types, as highlighted in yellow and green colors, respectively, in the BC map (Fig. 3c). For instance, grain G3 contains three variants, T_2, T_1 and T_4, with the latter two showing expanded interactions. Most of the grains that are unfavorable for tension twinning remain untwinned. However, in these tension-twin unfavorable grains, $\{10\bar{1}1\}$ compression twins and $\{10\bar{1}1\}$-$\{10\bar{1}2\}$ compression-tension (C-T) double twins (red arrows in the BC map in Fig. 3c) are detected due to their high SFs under pure shear. The occurrence of compression-tension double twins under pure shear at approximately half of the fracture strain is not observed in the case of uniaxial tension. Under uniaxial tension or compression, the C-T double twins are usually activated at the necking stage. The large shear localization of the double twin boundaries are thought to be responsible for the rapid final fracture [33,34]. Due to the absence of local necking in the torsion deformation, it might be reasonable to assume that the activation of double twins at the intermediate level of shear strain actually promotes accommodation of shear deformation rather than causes the premature fracture of the material.

As the shear strain is increased to γ_p=19.1% into Stage-IV (Fig. 3d), most of the grains favorable for tension twinning are fully twinned and the total TVF reaches 43.6%. For instance, grain G5 is almost fully twinned with T_1, T_4, and T_5. The profuse growth of different variants, such as T_1 and T_5 in grain G5, causes formation of extensive twin-twin boundaries. Also, the external stress at this stage is high enough to nucleate $\{10\bar{1}1\}$ compression twins in the favorable fully twinned areas, causing instances of $\{10\bar{1}2\}$-$\{10\bar{1}1\}$ tension-compression (T-C) double twins (such as T_5-C_2, blue area in the IPF map of grain G5) and $\{10\bar{1}2\}$-$\{10\bar{1}1\}$-$\{10\bar{1}2\}$ tension-compression-tension (T-C-T) tertiary twins (such as T_5-C_2-T_2 in grain G5). It is noted that the T-C double and T-C-T tertiary twins operated under pure shear have sizes relatively larger than those observed under the compression stress state [35]. In the tension-twin unfavorable grains, the $\{10\bar{1}1\}$ compression twins and $\{10\bar{1}1\}$-$\{10\bar{1}2\}$ compression-tension double twins are persistently nucleated, *e.g.*, C_5, and C_5-T_5, in grain G6.

Finally, the microstructure near the end of Stage IV, at γ_p=25.4%, is presented in Fig. 3e. As anticipated, the continued shear straining leads to persistent nucleation and growth of multiple secondary T-C and tertiary T-C-T twin variants in the tension-twin favorable grains. For instance, grain G7 shows five bands of the T_3-C_1-T_1 tertiary twin and one band of the T_3-C_4-T_2 tertiary twin. In the grains unfavorable for tension twinning (such as grain G8), interaction of secondary compression-tension twin variants could be detected (such as C_2-T_2 and C_4-T_6). Since γ_p=25.4% is close to the fracture strain, a few micro-cracks sites (see the black area in grain G7) are detected at the intersection point of twin tip and grain boundary where stress concentration is localized. The twins which show micro-cracks at their tips are usually tertiary twins that have experienced three orders of sequential twinning and have

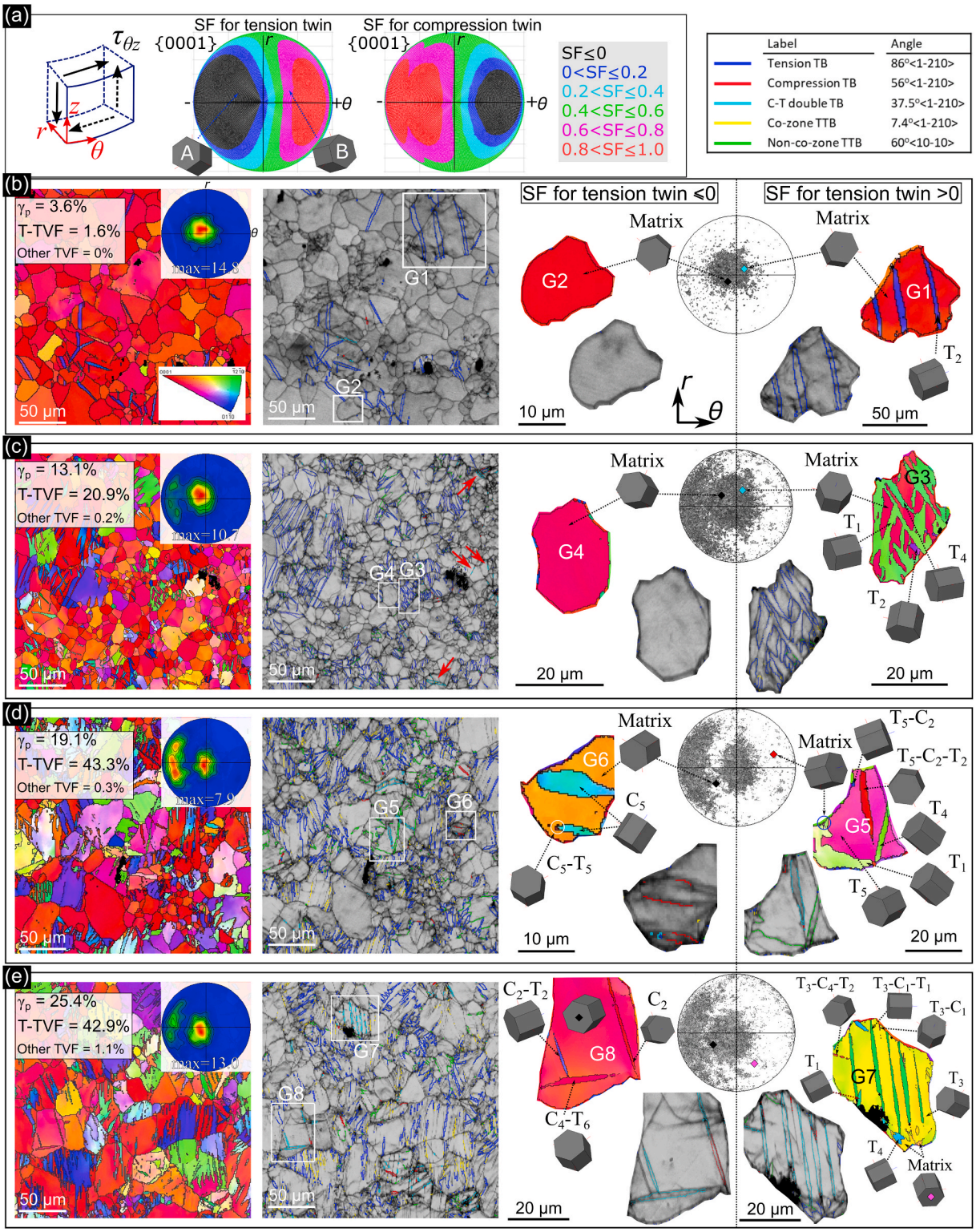

Fig. 3. Microstructure evolution characterized by EBSD at four shear strain levels in the rolled AZ31B magnesium alloy subjected free-end torsion about the normal direction in a rolled plate. (a) Schmid factor (SFs) pole figures for tension and compression twinning under pure shear stress state. (b–e) The deformed microstructure characterized at plastic shear strains of 0.036, 0.069, 0.131, 0.191, and 0.254, respectively.

excessive shear localization of their twin boundaries. This implies that shear localization of twin boundaries is a controlling factor for the final fracture Mg alloys under shear stress state. However, in contrast to the uniaxial loading, larger fracture strain can be attained under shear due to the lack of necking in the specimen under torsional loading. The exact fracture mechanism under torsion should be further investigated.

3.3. *Swift effect under free-end torsion*

The Swift effect, which is often observed in cubic-structured metals such as stainless steel, aluminum, copper, and brass [27], is mainly attributed to the accumulation of dislocation slips in the textured microstructure that contributes to the axial elongation during free-end

torsion deformation. As confirmed from Fig. 2, the Swift effect is clearly evidenced in the current study. The existing studies attribute the Swift effect in *hcp* Mg mainly to tension twinning with a high dependence on the initial texture [14]. In the current study, the original microstructure of the rolled AZ31B plate has the most grains with their *c*-axes oriented along with the ND. As a result, the material provides an ideal basal texture to verify the origin of the Swift effect. Since tension twinning reorients the matrix about 86.3° and induces a misfit strain ε_{misfit}along the *c*-axis or ND [36] (Fig. 4a), a twinning-induced axial strain (ε_{twin}) along the ND (Fig. 4a) for the experiments conducted in the current study can be approximated as:

$$\varepsilon_{twin} = \mathrm{TVF} \times \varepsilon_{misfit} \quad (1)$$

where TVF is the tension twin volume fraction, $\varepsilon_{misfit} = (\sqrt{3} - \lambda)/\lambda$is the misfit strain along the *c*-axis generated by twinning [36], $\lambda$is the *c*/*a*ratio. For Mg alloys,$\lambda = \frac{c}{a} = 1.624$, and therefore,$\varepsilon_{misfit} = 0.067$. As summarized in Fig. 4b, the tension TVF increases from 1.6% at γ_p=3.6% to a saturation value of approximately 43% at γ_p=19.1%, and the value remains almost unchanged until fracture. Therefore, the contribution of tension twinning to the axial strain (ε) can be evaluated by the ratio $\varepsilon_{twin}/\varepsilon$as a function of plastic shear strain (Fig. 4b). At a low plastic shear strain level (γ_p= 3.6%), the contribution of twinning takes only ~20%, thus the axial elongation is mostly due to dislocation slips. However, at a plastic shear strain higher than 3.6%, the contribution of twinning to the axial strain lies in the range between 80% and 100%, inferring that twinning accommodates most of the axial elongation. This result confirms that tension twinning plays a major role in the Swift effect in Mg alloys, in particular at large shear deformation.

3.4. Role of twinning in strain hardening rate

As revealed from the relative activities of slip/twinning predicted by crystal plasticity modeling of free-end torsion of AZ31B plate about the ND [14], basal slips and tension twinning act as the major deformation modes throughout the torsion deformation due to their relative low CRSS. Prismatic <*a*> slips become significant only at a large shear strain particularly higher than ~12%. The operation of non-basal prismatic slips at large shear deformation promotes the shear plasticity and can lead to a reduction of the strain hardening rate [37]. This explains well the observed decreasing strain hardening rate during Stage IV deformation in the torsion experiments (Fig. 2). Nevertheless, it is more interesting to note that a two-stage rise of the strain hardening rate is observed during Stage II & III deformation, where only basal slips and tension twinning are mainly operated. As basal slips and tension twinning have low CRSS and can be activated easily, it is speculated that the observed rise of the hardening rate is associated with unique twinning behavior and the hardening effects occurring under torsion in the current study.

To explore the hardening behavior, the length fraction of each type of TBs as a function of the shear plastic strain is analyzed. The TBs include primary tension TB (86°<1$\bar{2}$10>), compression TB (56°<1$\bar{2}$10>), and compression-tension double TB (37.5°<1$\bar{2}$10>). Such an analysis is also conducted for every type of TTBs, including co-zone TTB (7.4°<1$\bar{2}$10>) and non-co-zone TTB (60°<10$\bar{1}$0>).

Fractions of each TB and TTB relative to their total lengths are summarized in Fig. 5. The tension TB fraction initially increases to ~24% at = γ_p~7% and then decreases monotonically to ~13% at fracture. The decreasing tension TB is ascribed to the formation of TTBs during the expansion of tension twins within the grain interior, as shown clearly in Fig. 3, particularly at a large plastic strain. In contrast to the profuse tension TBs, the fractions of compression TB and compression-tension double TB are much fewer in amount, increased to their maximum values of 0.5%, and 1.5%, respectively, at fracture. As for the variation of TTBs, the total fraction of TTBs increases from 0 at = γ_p~7%–~2.6% at = γ_p~19%, and remains almost constant during the rest of deformation, where the non-co-zone TTB takes about ~84% of the total TTB fraction.

Early studies have shown that TBs and TTBs can act similar to grain boundaries as sites for dislocation pile-up and storage, and play a role of strain hardening in terms of blocking dislocation motion [38]. Recently, it is revealed that formation of TTBs, in particular of the non-co-zone

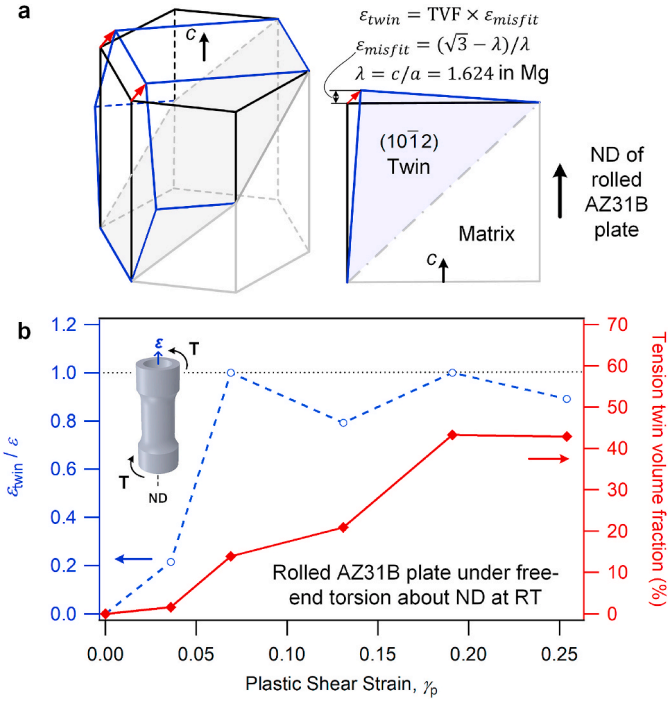

Fig. 4. Verification of Swift effect by evaluating the contribution of {10$\bar{1}$2} tension twinning to the axial strain: (a) Schematic showing the misfit strain along the *c*-axis induced by tension twins. (b) The ratio of twinning-induced axial strain to the experimentally measured axial strain ($\varepsilon_{twin}/\varepsilon$) and the tension twin volume fraction as a function of plastic shear strain during free-end torsion of rolled AZ31B about the ND.

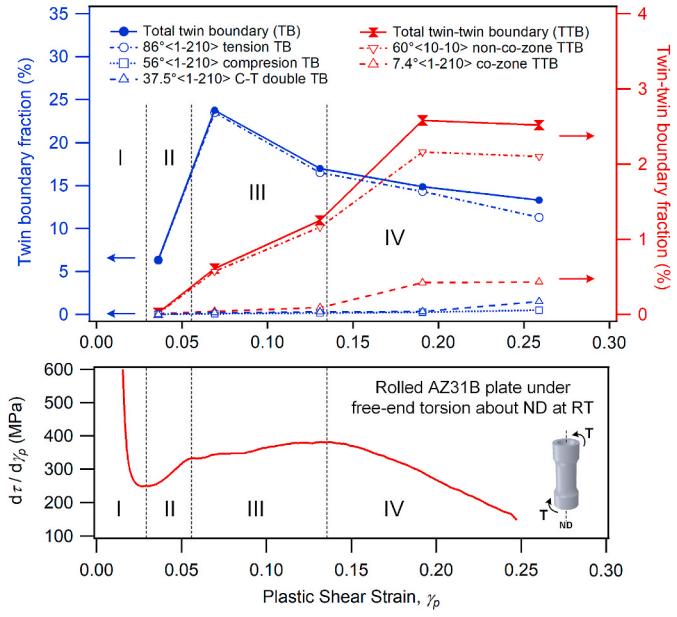

Fig. 5. Length fractions of twin boundaries and twin-twin boundaries as a function of plastic shear strain during free-end torsion of AZ31B Mg alloy about the normal direction of the rolled plate.

type, is energetically unfavorable, which requires additional work hardening supplied by external loading [32,39,40]. Therefore, as compared to the TBs, TTBs not only play a role to inhibit dislocation motion but also contribute to additional hardening even during their formation process. This hardening effect by TTB formation is clearly manifested as the continued rise of the strain hardening rate in Stage II & III deformation, during which TTB fraction increases continuously, indicating a sustained formation of TTBs. The slow rise of the strain hardening rate in Stage III as compared to that in Stage II can be explained by the decreased barrier effects of TBs to dislocation motion due to the reduction of TBs fraction caused by multiplication of TTBs (Fig. 5).

It is clear that the barrier effects of TBs and TTBs to dislocation motion and the energetically unfavorable formation of TTBs collectively contribute to the rising strain hardening rates in Stage II & III. This unique strain hardening behavior leads to a subtle sigmodal shape exhibited in the shear stress-strain curves (Fig. 2). During Stage IV, the hardening effect ascribed to TTB formation diminishes as the generation of TTBs approaches exhaustion. Although TBs and TTBs still act to inhibit dislocation motion, the role of non-basal prismatic slips becomes more significant at large shear deformation because of the increased shear stress [14]. As discussed earlier, the operation of non-basal slips effectively results in a reduction in strain hardening rate, which is regarded as the main reason for the reduction of hardening rate in Stage IV observed in the experiments in the current study.

4. Conclusions

Free-end torsion experiments were conducted on the thin-walled tubular specimen with the torsion axis aligned parallel to the normal direction (ND) of a rolled AZ31B Mg alloy plate. The stress-strain response and the microstructure evolution were characterized as a function of increasing strain in detail with an emphasis to understand the role of deformation twins. Key findings are listed as follows:

1. The shear stress-shear strain response shows a subtle sigmodal shape. The shape is associated with four distinct stages of strain hardening: rapid decrease due to macroscopic yielding (Stage I), fast rise (Stage II), slow rise (Stage III), and progressive decrease (Stage IV).
2. Under pure shear stress state, both tension twinning and compression twinning are favored. With increasing shear strain, multiple tension twin variants and twin-twin interactions are frequently observed. In the tension-twin favorable grains, double T-C and tertiary T-C-T twins of detectable sizes are observed at a shear strain of approximately 50% of the fracture strain. Conversely, primary compression twin and C-T double twins are only detected in tension-twin unfavorable grains.
3. An axial strain of 3.5% is developed under free-end torsion confirming the occurrence of Swift effect. The origin of Swift effect is attributed to the dislocation slips at a shear strain less than 5% but predominantly due to tension twinning at a larger plastic strain.
4. Basal slips and tension twinning are operated throughout the shear deformation. The rise of strain hardening rate during Stage II & III is attributed to the collective hardening by the inhibiting effect of TBs and TTBs to dislocation motion and the energetically unfavorable TTB formation. In Stage IV, non-basal prismatic slips whose role becomes more significant as TTB formation exhausts is responsible for the progressive decrease in strain hardening rate.

Data availability

The raw/processed data required to reproduce these findings cannot be shared at this time due to technical or time limitations.

Declaration of competing interest

The authors declare that they have no known competing financial interests or personal relationships that could have appeared to influence the work reported in this paper.

Acknowledgment

The research was supported by the U.S. National Science Foundation (CMMI-1762312).

References

[1] I.J. Polmear, Magnesium alloys and applications, Mater. Sci. Technol. 10 (2012) 1–16, https://doi.org/10.1179/026708394790163401.
[2] M. Barnett, Influence of deformation conditions and texture on the high temperature flow stress of magnesium AZ31, J. Light Met. 1 (2001) 167–177, https://doi.org/10.1016/S1471-5317(01)00010-4.
[3] B.C. Wonsiewicz, A. Backofen, Plasticity of magnesium crystals, Trans. Metall. Soc. AIME. 239 (1967) 1422–1431.
[4] X.Y. Lou, M. Li, R.K. Boger, S.R. Agnew, R.H. Wagoner, Hardening evolution of AZ31B Mg sheet, Int. J. Plast. 23 (2007) 44–86, https://doi.org/10.1016/j.ijplas.2006.03.005.
[5] J.-Y.Y. Kang, B. Bacroix, R. Brenner, Evolution of microstructure and texture during planar simple shear of magnesium alloy, Scripta Mater. 66 (2012) 654–657, https://doi.org/10.1016/j.scriptamat.2012.01.040.
[6] H. Zhang, G. Huang, L. Wang, H.J. Roven, Z. Xu, F. Pan, Improved ductility of magnesium alloys by a simple shear process followed by annealing, Scripta Mater. 69 (2013) 49–52, https://doi.org/10.1016/j.scriptamat.2013.03.011.
[7] B. Beausir, L.S. Tóth, F. Qods, K.W. Neale, Texture and mechanical behavior of magnesium during free-end torsion, J. Eng. Mater. Technol. Trans. ASME. 131 (2009), 0111081–01110815, https://doi.org/10.1115/1.3030973.
[8] P.D. Wu, H. Wang, K.W. Neale, On the large strain torsion of HCP polycrystals, Int. J. Appl. Mech. 4 (2012) 1–27, https://doi.org/10.1142/S175882511250024X.
[9] J. Hu, H. Gao, Y. Meng, Z. Zhang, L. Gao, Effects of free-end torsion on the microstructure evolution and fatigue properties in an extruded AZ31 rod, Mater. Sci. Eng. 726 (2018) 215–222, https://doi.org/10.1016/j.msea.2018.04.078.
[10] A.A. Roostaei, H. Jahed, Multiaxial cyclic behaviour and fatigue modelling of AM30 Mg alloy extrusion, Int. J. Fatig. 97 (2017) 150–161, https://doi.org/10.1016/j.ijfatigue.2016.12.037.
[11] D. Toscano, S.B. Behravesh, S.K. Shaha, H. Jahed, B. Williams, Characterization of closed-die forged AZ31B under pure axial and pure shear loading, Int. J. Fatig. 139 (2020) 105754, https://doi.org/10.1016/j.ijfatigue.2020.105754.
[12] A. Gryguć, S.B. Behravesh, S.K. Shaha, H. Jahed, M. Wells, B. Williams, X. Su, Multiaxial cyclic behaviour of extruded and forged AZ80 Mg alloy, Int. J. Fatig. 127 (2019) 324–337, https://doi.org/10.1016/j.ijfatigue.2019.06.015.
[13] S. Biswas, B. Beausir, L.S. Toth, S. Suwas, Evolution of texture and microstructure during hot torsion of a magnesium alloy, Acta Mater. 61 (2013) 5263–5277, https://doi.org/10.1016/j.actamat.2013.05.018.
[14] X.Q. Guo, W. Wu, P.D. Wu, H. Qiao, K. An, P.K. Liaw, On the Swift effect and twinning in a rolled magnesium alloy under free-end torsion, Scripta Mater. 69 (2013) 319–322, https://doi.org/10.1016/j.scriptamat.2013.05.010.
[15] J. Wang, D. Zhang, Y. Li, Z. Xiao, J. Fouse, X. Yang, Effect of initial orientation on the microstructure and mechanical properties of textured AZ31 Mg alloy during torsion and annealing, Mater. Des. 86 (2015) 526–535, https://doi.org/10.1016/j.matdes.2015.07.113.
[16] B. Song, C. Wang, N. Guo, H. Pan, R. Xin, Improving tensile and compressive properties of an extruded AZ91 rod by the combined use of torsion deformation and aging treatment, Materials 10 (2017) 3–8, https://doi.org/10.3390/ma10030280.
[17] N. Guo, B. Song, C. Guo, R. Xin, Q. Liu, Improving tensile and compressive properties of magnesium alloy rods via a simple pre-torsion deformation, Mater. Des. 83 (2015) 270–275, https://doi.org/10.1016/j.matdes.2015.06.071.
[18] J. Wang, X.Y. Yang, Y. Li, Z.Y. Xiao, D.X. Zhang, T. Sakai, Enhanced ductility and reduced asymmetry of Mg-2Al-1Zn alloy plate processed by torsion and annealing, Trans. Nonferrous Met. Soc. China (English Ed. 25 (2015) 3928–3935, https://doi.org/10.1016/S1003-6326(15)64040-7.
[19] F. Kabirian, A.S. Khan, T. Gnäupel-Herlod, Visco-plastic modeling of mechanical responses and texture evolution in extruded AZ31 magnesium alloy for various loading conditions, Int. J. Plast. 68 (2015) 1–20, https://doi.org/10.1016/j.ijplas.2014.10.012.
[20] B. Song, N. Guo, R. Xin, H. Pan, C. Guo, Strengthening and toughening of extruded magnesium alloy rods by combining pre-torsion deformation with subsequent annealing, Mater. Sci. Eng. (2016), https://doi.org/10.1016/j.msea.2015.10.069.
[21] J. Albinmousa, H. Jahed, S. Lambert, Cyclic behaviour of wrought magnesium alloy under multiaxial load, Int. J. Fatig. 33 (2011) 1127–1139, https://doi.org/10.1016/j.ijfatigue.2011.01.009.
[22] J. Zhang, Q. Yu, Y. Jiang, Q. Li, An experimental study of cyclic deformation of extruded AZ61A magnesium alloy, Int. J. Plast. 27 (2011) 768–787, https://doi.org/10.1016/j.ijplas.2010.09.004.

[23] J. Albinmousa, H. Jahed, S. Lambert, Cyclic axial and cyclic torsional behaviour of extruded AZ31B magnesium alloy, Int. J. Fatig. 33 (2011) 1403–1416, https://doi.org/10.1016/j.ijfatigue.2011.04.012.
[24] Q. Yu, J. Zhang, Y. Jiang, Q. Li, Multiaxial fatigue of extruded AZ61A magnesium alloy, Int. J. Fatig. 33 (2011) 437–447, https://doi.org/10.1016/j.ijfatigue.2010.09.020.
[25] Y. Xiong, Q. Yu, Y. Jiang, Multiaxial fatigue of extruded AZ31B magnesium alloy, Mater. Sci. Eng. 546 (2012) 119–128, https://doi.org/10.1016/j.msea.2012.03.039.
[26] H. Li, G. Kang, Y. Liu, H. Jiang, Non-proportionally multiaxial cyclic deformation of AZ31 magnesium alloy: experimental observations, Mater. Sci. Eng. 671 (2016) 70–81, https://doi.org/10.1016/j.msea.2016.06.043.
[27] H.W. Swift, Length changes in metals under torsional overstrain, Engineering 163 (1947) 253.
[28] H. Wang, P.D. Wu, J. Wang, Modelling the role of slips and twins in magnesium alloys under cyclic shear, Comput. Mater. Sci. 96 (2015) 214–218, https://doi.org/10.1016/j.commatsci.2014.09.015.
[29] Q. Yu, J. Zhang, Y. Jiang, Fatigue damage development in pure polycrystalline magnesium under cyclic tension–compression loading, Mater. Sci. Eng. 528 (2011) 7816–7826, https://doi.org/10.1016/j.msea.2011.06.064.
[30] J. Zhang, Q. Yu, Y. Jiang, Q. Li, An experimental study of cyclic deformation of extruded AZ61A magnesium alloy, Int. J. Plast. 27 (2011) 768–787, https://doi.org/10.1016/j.ijplas.2010.09.004.
[31] B. Song, N. Guo, R. Xin, H. Pan, C. Guo, Strengthening and toughening of extruded magnesium alloy rods by combining pre-torsion deformation with subsequent annealing, Mater. Sci. Eng. 650 (2016) 300–304, https://doi.org/10.1016/j.msea.2015.10.069.
[32] Q. Yu, J. Wang, Y. Jiang, R.J. McCabe, N. Li, C.N. Tomé, Twin–twin interactions in magnesium, Acta Mater. 77 (2014) 28–42, https://doi.org/10.1016/j.actamat.2014.05.030.
[33] M.R. Barnett, Twinning and the ductility of magnesium alloys Part II. Contraction Twins, Mater. Sci. Eng. 464 (2007) 8–16, https://doi.org/10.1016/j.msea.2007.02.109.
[34] D. Ando, J. Koike, Y. Sutou, Relationship between deformation twinning and surface step formation in AZ31 magnesium alloys, Acta Mater. 58 (2010) 4316–4324, https://doi.org/10.1016/j.actamat.2010.03.044.
[35] Q. Yu, Y. Jiang, J. Wang, Tension-compression-tension tertiary twins in coarse-grained polycrystalline pure magnesium at room temperature, Phil. Mag. Lett. 95 (2015) 194–201, https://doi.org/10.1080/09500839.2015.1022621.
[36] B. Li, X.Y. Zhang, Global strain generated by shuffling-dominated $\{10\bar{1}2\}<10\bar{1}\bar{1}>$ twinning, Scripta Mater. 71 (2014) 45–48, https://doi.org/10.1016/j.scriptamat.2013.10.002.
[37] J. Koike, Enhanced deformation mechanisms by anisotropic plasticity in polycrystalline Mg alloys at room temperature, Metall. Mater. Trans. A Phys. Metall. Mater. Sci. 36 (2005) 1689–1696, https://doi.org/10.1007/s11661-005-0032-4.
[38] S.G. Song, G.T. Gray, Influence of temperature and strain rate on slip and twinning behavior of Zr, Metall. Mater. Trans. 26 (1995) 2665–2675, https://doi.org/10.1007/BF02669423.
[39] Q. Yu, J. Wang, Y. Jiang, R.J. McCabe, C.N. Tomé, Co-zone (1012) twin interaction in magnesium single crystal, Mater. Res. Lett. 2 (2014) 82–88, https://doi.org/10.1080/21663831.2013.867291.
[40] L. Jiang, J.J. Jonas, A.A. Luo, A.K. Sachdev, S. Godet, Influence of {10-12} extension twinning on the flow behavior of AZ31 Mg alloy, Mater. Sci. Eng., A (2007), https://doi.org/10.1016/j.msea.2006.09.069.